Fusion Engineering and Design 205 (2024) 114534

Contents lists available at ScienceDirect

Fusion Engineering and Design

journal homepage: www.elsevier.com/locate/fusengdes

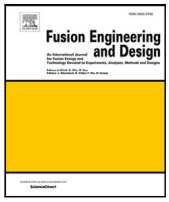

Advancing MARFE detection in JET's operational camera videos through Machine Learning techniques

A. González Ganzábal [a,b,*], G.A. Rattá [a], D. Gadariya [a], S. Dormido-Canto [c], JET Contributors [1]

[a] Laboratorio Nacional de Fusión, Spain
[b] Universidad Nacional de Educación a Distancia, Spain
[c] Dpto. Informática y Automática, Universidad Nacional de Educación a Distancia, Spain

ARTICLE INFO

Keywords:
JET
Machine learning
MARFE
Operational cameras
Video detection
Visible cameras

ABSTRACT

In order to prove the capability of operational cameras in nuclear fusion devices, the videos from the cameras at JET were used to detect the occurrence of MARFEs, an edge plasma phenomenon. Three techniques were tested in this work: two already reviewed in other publications and a new one based on intensity masks. Once these methods were validated, their output was used to develop several Machine Learning models to improve performance. A final Machine Learning model was devised using both data from the operational cameras and several signals and diagnostics from other instruments at JET. The outcomes achieved using all the methods presented were deemed satisfactory, leading to the final Machine Learning model exhibiting an impressive accuracy rate of 96.9%. Furthermore, the models allow for detection both in frame by frame (if only video data is used) and in 2 ms time steps should all diagnostics be used.

1. Introduction

In the realm of energy prospects, nuclear fusion emerges as the flagship of clean energy for the future. With its promise of being a sustainable and nearly limitless resource, nuclear fusion holds tremendous potential. This process involves the fusion of light elements, primarily helium (He), deuterium (^2H), and tritium (^3H), resulting in the release of vast amounts of energy. To recreate the extreme conditions necessary for these reactions, plasma — an ionised gas generated by electrical currents — is employed in experimental nuclear fusion devices. Among these devices, JET stands as the largest operational tokamak of its generation, before ITER and JT-60SA, which has started its operations recently. To gain a better understanding of various physical phenomena and develop effective control mechanisms, multiple diagnostic tools have been implemented. This paper will specifically explore the significance of operational cameras as valuable diagnostic tools.

Operational cameras possess substantial untapped informational value, despite being underutilised in comparison with other diagnostics in several nuclear fusion devices. In this paper, the value of these operational cameras for plasma diagnostics will be proven by analysing the detection of MARFEs (Multifacetic Asymmetric Radiation From the Edge[2]), an edge plasma phenomenon with data taken directly from JET's operational cameras.

After a brief introduction regarding MARFEs as a physical phenomenon and JET's operational cameras (Sections 1.1 and 1.2, respectively), this paper will delve into the construction process of the MARFE database in Section 2 and will examine various detection models developed exclusively for this work (see 2.1) or adapted from existing publications by other authors (2.2 and 2.3). Furthermore, models with Machine Learning architecture were also created and will be explored in Section 3. Subsequently, we present the derived results and conduct a comprehensive analysis of the predictions, drawing comparisons among them in Section 4. The final conclusions of this work can be found in Section 5.

1.1. MARFE

MARFEs are low-temperature, high-density regions that appear at the plasma periphery when the electron number density surpasses a critical threshold. Adjusting parameters such as the plasma current or reducing lighter impurities can increase this threshold as it was experimentally found [1]. Understanding these manipulations is crucial for studying MARFE properties and behaviour. Previous studies [1,2] have examined the effects of MARFE on the main and edge plasma, revealing significant changes in the peripheral region, but not so many in the

* Correspondence to: Av. Complutense, 40, Moncloa - Aravaca, 28040 Madrid, Spain.
E-mail address: alejandro.gonzalez@ciemat.es (A. González Ganzábal).

[1] See the author list in J. Mailloux et al. 2022 (https://doi.org/10.1088/1741-4326/ac47b4).

[2] See Appendix B for a list of all the acronyms used.

https://doi.org/10.1016/j.fusengdes.2024.114534
Received 15 November 2023; Received in revised form 27 February 2024; Accepted 31 May 2024
Available online 11 June 2024

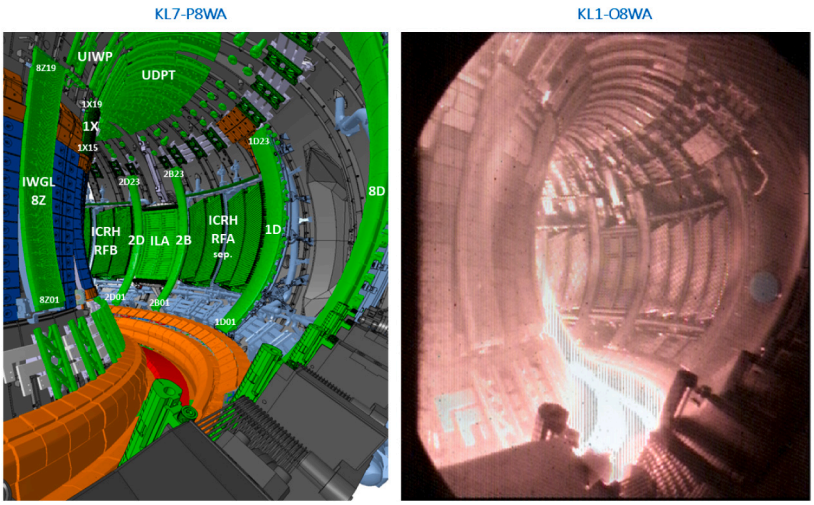

Fig. 1. Figure shows the view from the KL1-O8WA camera, alongside the schematic view inside the chamber. A review of the main areas present in the simplified view can be found in Appendix B, albeit not all of them are relevant for this work.

main area. In tokamaks, discharges with MARFEs are strongly linked with disruptions (a violent event in which the magnetically confined plasma is forced into termination as a consequence of instabilities) due to the action of neutral particles. These particles migrate towards the plasma edge region, triggering ionisation, charge exchange, and recombination processes [2], which can lead to instabilities and the plasma termination. The detection of MARFEs is crucial to avoid and control disruptions, a critical field of research, since these events may severely damage the nuclear device.

The shift in temperature results in a radiation flow that can be observed with the cameras of the device. Some authors [3–5] have already developed techniques that take advantage of the videos generated. Out of these, one has been replicated in this work and the other has been used as a starting point to develop a similar detection method. A third method based on intensity masks has also been developed ad-hoc for this paper. As a last step, and in order to improve the results of the 3 tested method, several Machine Learning models were trained and tested.

1.2. JET's operational cameras

Only one of the operational cameras, labelled KL1-O8WA [6], has been used for this work. This is a wide angle, COHU colour CCD-based camera that operates in the visible spectrum [7] with a frame rate of near 42 ms and a fixed resolution of 576 × 720 pixels. For each experiment produced in JET (usually called pulse or discharge), a video of 1050 frames is recorded. These videos can be synchronised with other real time signals and alerts by converting the frame rate into real time with 1D time arrays also available for each pulse. For the sake of simplicity, unless otherwise specified, whenever a video/video event is mentioned, it should be considered that it has been already properly synchronised. Fig. 1 [8] offers a visual glimpse into the captured video footage from these cameras, and it is accompanied by an illustrative scheme of the octant. In the KL7 view, the divertor (visually accentuated in orange) fulfils its purpose as a specialised segment within the vessel, tasked with waste collection. Within this context, the divertor serves as the focal point for observing the primary plasma dynamics under normal operational circumstances, channelling and absorbing the predominant heat load while ensuring the protection of critical neighbouring areas.

MARFEs and other instabilities will appear near the areas marked as IWGL (Inner Wall Guard Limiter) and UIWP (Upper Inner Wall Protector). In this paper, for the sake of simplicity, these zones will be labelled as the High Field (HF) area. Thus, in our case and as proof of principle, a MARFE occurrence will be characterised on video by a rapid flux of radiation from the divertor to the HF.

As an example, Fig. 2 depicts the observation of a MARFE: the radiation from the plasma moves quickly from the divertor area to the High Field (frames 2 to 4), and remains there for the rest of the pulse. An increase of intensity can be noticed once the MARFE has been set, starting from frame 13. To simplify the illustration, a selection of relevant frames was chosen to depict the sequence of interest while minimising the total number of frames presented.

In addition to the data from the operational cameras, and in order to evaluate how other signals and diagnostics can be used to improve the MARFE detection, other sources of data were used. A collection of other signals was added (see Appendix A), alongside several electron temperature curves and electron density profiles measured alongside different points over the radius of the torus. This combination of data from JET's signals and the videos from operational cameras has already been used in other analysis with good results [9].

These signals were resampled using interpolation with the previous neighbour, as other interpolation methods could potentially trigger an alarm without detecting proper anomalies accurately in one of JET's instruments. JET's alarms are managed through PETRA,[3] a security framework connected to JET's Real Time Protection Sequencer (RTPS), which prevents disruptions utilising mitigation processes [10] relying on real time data from its instruments. The signals were resampled with a time step of 2 ms, which is the same time step used by PETRA.

The importance of these operational cameras lies in three fundamental points:

- Economical Advantage: compared to the experimental cameras integrated within the JET framework, these operational devices present an economically convenient option. In terms of computational power and disk storage, operational cameras are also more convenient to work with, as the videos from experimental cameras can be up to 2.3 times larger and might not cover the complete duration of the discharge.
- Full Plasma Insight: operating within a broad field of view, these cameras comprehensively capture essential plasma data for diagnostic analysis. This obviates the need to depend on imagery from several video sources. More advanced cameras, like the experimental fast cameras that also capture the full view of the chamber do not record the whole pulse (such as KL8-EW8 A

[3] Plasma Events TRiggering Alarm.

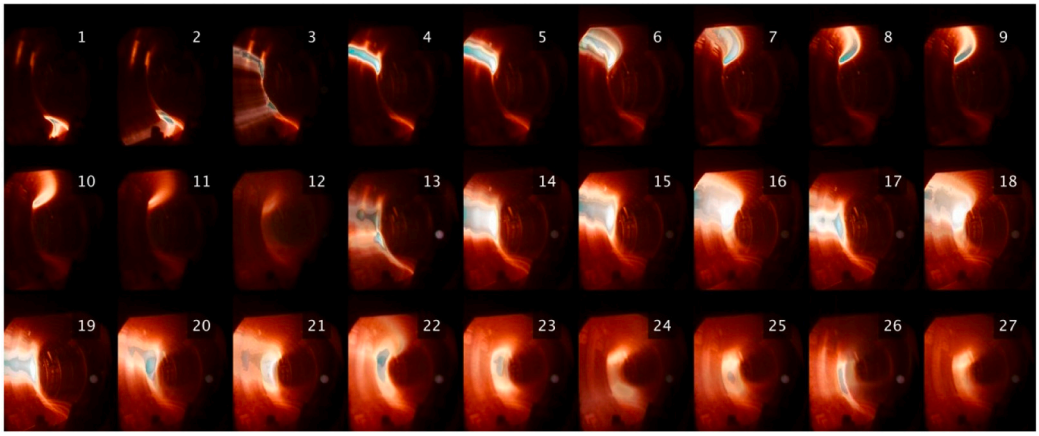

Fig. 2. Figure shows the record of a MARFE obtained from the JET camera for discharge 94 905.

or KLDT-E5WC) but simply a few seconds depending on the configuration that was set for the discharge (i.e: for pulse 94 626, the full discharge is recorded for KL1-O8WA and only half a second for KL1-E8WA).

- Simplicity: video acquisition by operational cameras is usually easier, which makes it possible to guarantee that the pulses have an associated video. Other more complex cameras do not have videos available for all discharges during the full pulse. The configuration for the operational cameras is not modified between pulses, thus guaranteeing homogeneity, which is vital for working with Machine Learning techniques.

2. Methodology and database

To develop and evaluate the methods proposed, we gathered a database with 104 pulses. Each discharge was meticulously analysed by manually examining video footage and assessing the Mode-Lock signal and the plasma current. Special attention was put into identifying the starting and finishing times of sudden changes correlated with observed instabilities in the High Field. Among the 104 pulses, 27 showed no visible MARFE. In case of doubt, and to ensure proper diagnostic of a MARFE occurrence, the session logs for the discharges were also consulted.

After completing the dataset, three methodologies based entirely on direct experimentation with the videos were developed and evaluated. To refine each technique, 80 discharges were carefully selected, while the remaining 24 discharges were used for testing. These approaches utilise direct data from the video to make the MARFE detection. After the detection, all the data that has been used is stored into files that can be used for new Machine Learning techniques (see Section 3). All these methods produce a binary alarm (1 for presence, 0 for absence) indicating the presence of a MARFE in a discharge and a binary array that uniformly classifies all video frames for every pulse that can be easily synchronised in time with the video and other physical events.

2.1. Method 1: analysis of intensity masks

This method consists on evaluating the average intensity of the video frame by frame in two separated masks. One of the masks evaluates the divertor area, which is where most of the intensity is focused under normal conditions in the video, while the second mask focuses on assessing the High Field region, which is more susceptible to the occurrence of MARFEs.

To create these masks, the videos of several discharges were evaluated. First, the divertor mask was created by grouping several frames right before a MARFE by multiplying the image matrices. This will be referred as the divertor mask. Similarly, the frames after a MARFE of each pulse were selected and added in a similar way. The divertor mask was subtracted from this MARFE mask to avoid confusion. A noise threshold was imposed to both resulting images. Finally, the two masks were binarised by applying an auto-clustering algorithm to both images.

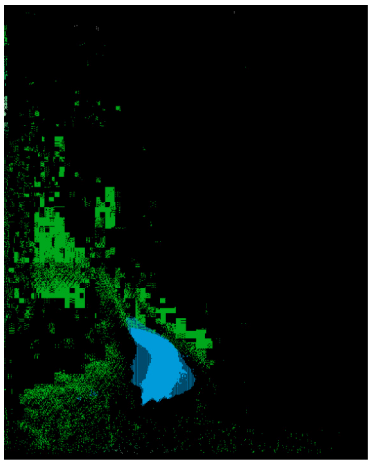

Fig. 3. The figure shows the two masks used in the process of detection via masks. The blue mask corresponds to the divertor mask, and the green mask corresponds to the MARFE mask.

In the analysis process, both masks are applied to each frame of the video. The occurrence of a MARFE/HF instability is anticipated when the average intensity of the MARFE mask exceeds that of the divertor mask. Fig. 3 visually depicts the appearance of both masks on a single video frame, utilising a two-colour scheme to differentiate between them.

An example of how this technique operates with a discharge can be seen in Fig. 6(a).

2.2. Method 2: analysis of regions of interest

For this method, the technique published in [3] has been reproduced. This approach is based on the analysis over time of the average intensity of certain ROIs (Regions Of Interest of size 2 × 2 pixels) distributed over all video frames. The positions and sizes of the ROIs are the same as in the original paper [3], which used genetic algorithms to search the optimal sizes and placements. The average intensities of the ROIs are then evaluated over time for all video frames, and whenever a shift of intensity is detected for one or several ROIs with respect to the one from the divertor, a MARFE/HF phenomena is considered for

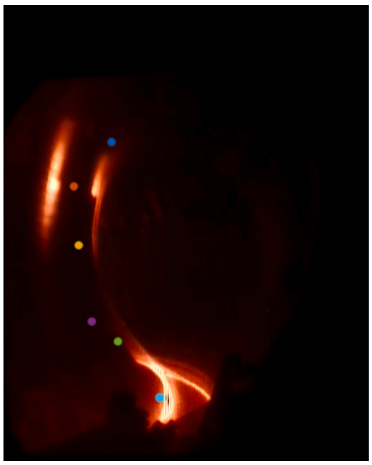

Fig. 4. Figure shows one video frame in which each ROI has been marked. Although the size of each ROI is 2 × 2 pixels, the area marked is bigger to make it easier to spot.

these frames. The different ROIs are shown in a video frame in Fig. 4, following the colour scheme used in its plotting example in Fig. 6(b).

It should be noted that with both this method and the one described in 2.1, a standard normalisation procedure was performed to scale the measures (simply dividing them by 255). The results do not change if a normalisation process is applied, as the rules for a detection are based on intensity shifts and their ratio to a general threshold. For values below that threshold, the intensity is not evaluated, as it is considered noise.

2.3. Method 3: analysis of KNN-based regions

This approach employs a K-Nearest Neighbors (KNN) algorithm to divide frames into two distinct regions based on their brightness levels. The KNN algorithm separates a set of data points into K non-overlapping clusters based on the likelihood of each element of belonging to a certain cluster [11].[4] It measures intensity, centroid displacement, and number of pixels in the brightest KNN region within the High Field, marked as a rectangular mask created manually to define this area. It is an updated version of a previously published method [5], with additional information for improved detection. This method considers an HF phenomenon whenever there is a shift in intensity between the high field and the outer part of the frame, an overlap between the HF and the bright region (measured in number of pixels) and a sudden change in the position of the intensity region centroid. Unlike other approaches, it evaluates intensity, position, and displacement modulus of the region, not just the displacement magnitude.

Two preprocessing techniques for the video frames were considered for this method in order to check if detection could be enhanced:

1. Whether or not use normalisation: as mentioned above, normalisation would allow to use this method in real time. To evaluate this proposal, a set of maxima and minima values was obtained by running the algorithm with 30 pulses. These values were used to normalise the output value for each frame.
2. Whether or not performing denoising techniques to each frame in order to improve the results. The algorithm chosen was 'wiener2', which compares the statistical information of each pixel and its surroundings with the statistics of the complete image to produce a filtered image through estimation [12], similar to signal processing denoising techniques. A comparison between a video frame with and without running the denoising algorithm can be seen in Fig. 5.

[4] See Chapter 10.3.1.

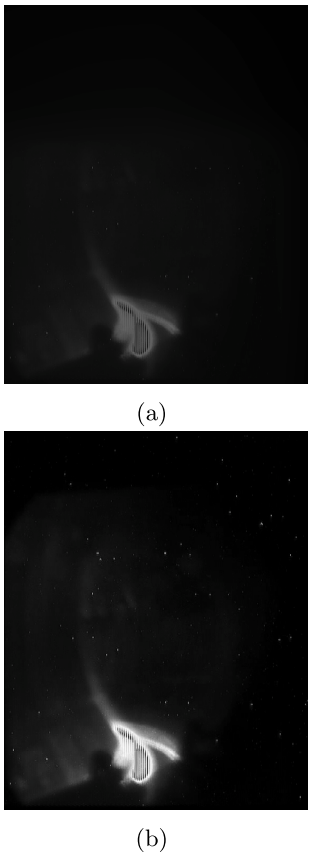

Fig. 5. The Figures show a comparison between the same video frame with 5(a) and without 5(b) running the denoising algorithm.

None of these two considerations seemed to improve the detection rates, so the definitive KNN regions were created without normalising and without the denoising algorithm.

2.4. Example of MARFE detections

The output for the three aforementioned models can be seen in Fig. 6, alongside all the variables used for the prediction. In the Figure, the three methods are compared in time, highlighting the detected MARFE at roughly the same time (near $t \approx 54.5$ s). Thus, in Fig. 6(a) the MARFE is detected when the intensity of the HF mask surpasses the intensity of the divertor mask. In Fig. 6(b) the intensity of the ROI corresponding to the divertor decreases drastically and it is surpassed by the intensity of the ROIs located over the IWGL. The pixel coordinates shown in the legend of Fig. 6(b) are referred to the video frame coordinates, as seen in Fig. 4 and uses the same colour scheme.

Lastly, in Fig. 6(c) the intensities inside and outside the HF are shown, as well as the number of pixels inside the HF and the modulus of the displacement vector of the centroid. It should be noted that these variables have been normalised for easier representation. It can be seen how the data registered from the intensities correlates with changes in the KNN-generated bright region and with the MARFE detection times, as expected.

In all three detection methods, there is a small increase in the intensity of the divertor area after the first MARFE detection. This phenomenon may arise because the MARFEs are not effectively stabilised within the HF; instead, they oscillate between the HF and the divertor regions. This is why a correction routine is executed to

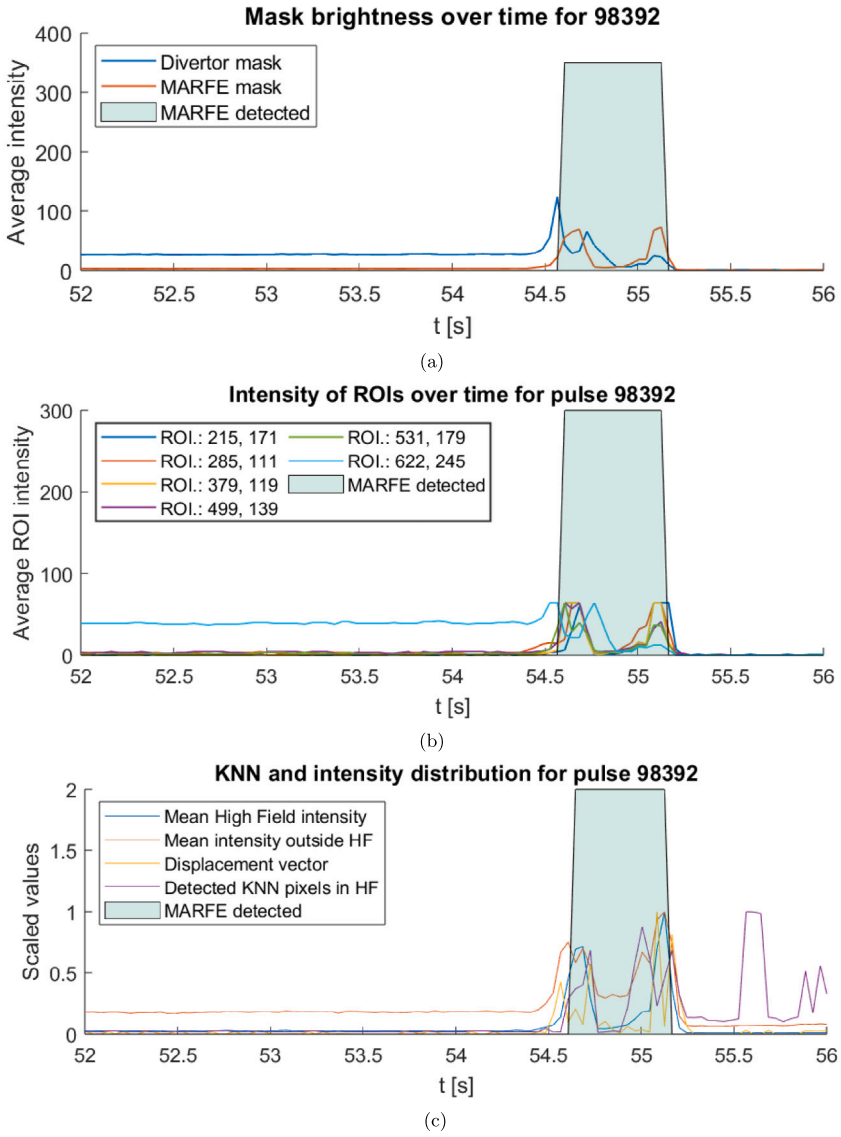

Fig. 6. Examples of the three methods used for non-statistical detection for a given pulse, in this case, 98 392. 6(a) corresponds to the mask method, 6(b) depicts the ROI method, and 6(c) refers to the KNN method.

avoid disjointed detection times (cases with consecutives zeros and ones that might arise due to noise or other factors without any further utility or physical meaning), which produces smooth and homogeneous detection intervals.

3. The machine learning techniques

After executing all the existing methodologies on the complete dataset and with the objective of obtaining better and more detailed results, three distinct Machine Learning models were formulated. These models use the binary results from the predictions produced by each method to classify pulses 3.1 and the frame-by-frame data generated for each discharge (3.2, 3.3), respectively. This data is stored in separate files created every time a discharge is evaluated with the methods described before (2.1, 2.2, 2.3) and contains the information used in each method. The architectures of the models, as well as their hyperparameters, were obtained by optimisation functions.

3.1. Binary model

The first model implemented is built upon a kernel logistic regression framework. Logistic regression is a Machine Learning technique that estimates the probability for a given data point of belonging to a certain class using a linear regression. By also using the kernel approach, the data points are first portrayed in a higher dimensional space [11].[5]

The objective of this model is to classify individual pulses into two categories: those exhibiting a MARFE (1) and those that do not (0). This model utilises the three final binary outputs obtained from the previous methods as input features. The purpose of this approach is to address any potential biases inherent in each individual technique by aggregating their final predictions. Consequently, the model is trained using a dataset comprising the 104 observations, which are divided into a 70% training set and a 30% testing set (including 8-fold cross validation). Thus, each of the 104 observations will be characterised by the three final binary alarms of the methods described in 2.

[5] See Chapter 4.3: Linear Regression.

3.2. Video-based models

A second model, in this case, a neural network, was developed with a database created with all the video data extracted by the non-statistical approaches, which allowed to create a larger dataset capable of frame-by-frame MARFE detection, instead of relying on classifying entire discharges. This database consists of 1854 observations, 861 of these being labelled as having MARFEs, with a total of 10 feature vectors per discharge:

- Columns 1–2: the mean intensities of the MARFE mask and the divertor mask for each frame.
- Columns 3–8: the mean intensity over time for each ROI for each frame.
- Columns 9–10: the modulus of the displacement of the bright KNN region and the number of pixels in the bright KNN region that overlap with the High Field region.

The intensities used in the KNN-based method were neglected, as they were deemed redundant, since both the mask and ROI approach already made use of average intensity values. The neural network has a single fully connected hidden layer with 188 neurons with a *relu* activation for the hidden layer and a *softmax* activation for the output layer.

To compensate for the more computationally demanding KNN-based method, a second neural network was created with the same database as the prior model. In this case, only the intensities from the masks and ROI approaches (8 feature vectors for 1854 observations) were considered. Both neural networks employ a 70%/30% training-test split, with a 20-fold cross validation set. The resulting architecture of the neural network consists of three fully connected hidden layers with sizes 147-1-4, with an hyperbolic tangent activation function and again, a *softmax* output activation, with a LBFGS optimiser.

3.3. "Comprehensive" model

A third and final Machine Learning method, this time with a KNN (not to be mistaken with the method presented in 2.3) architecture was devised. This time, the video data from all the aforementioned techniques is used alongside the data from several diagnostics and signals from other instruments at JET, including electron temperature curves and electron number densities profiles over several lengths over the torus. An example of some of these signals can be found in Fig. 7.

All the data for this model has been resampled to 2 ms time step as mentioned in 1.2. The final, normalised datasets for every pulse have the following structure:

1. From columns 1 to 28: feature vectors from several JET instruments and alarms. The complete list can be found in Appendix A.
2. From columns 29 to 40: the data extracted from using the three video-based algorithms. These are the same feature vectors that have been used in 3.2.
3. Columns 41 to 103: the electron temperature curves.
4. Columns 104 to 166: the electron number density profiles.
5. Column 167: target variable: 1 if MARFE, 0 otherwise.

Unfortunately, since not all the desired signals are available for all the JET discharges presented in the database, some pulses had to be removed. This final database contains a total of 1509 observations (761 with MARFE, 748 without) from 69 discharges, with a train–test split of 70%–30% with a 20-fold cross validation batch.

4. Results

The forthcoming section delves into the outcomes derived from the aforementioned methodologies elucidated in the preceding chapters. Furthermore, this section encompasses supplementary observations and comprehensive conclusions that can be gleaned from each method.

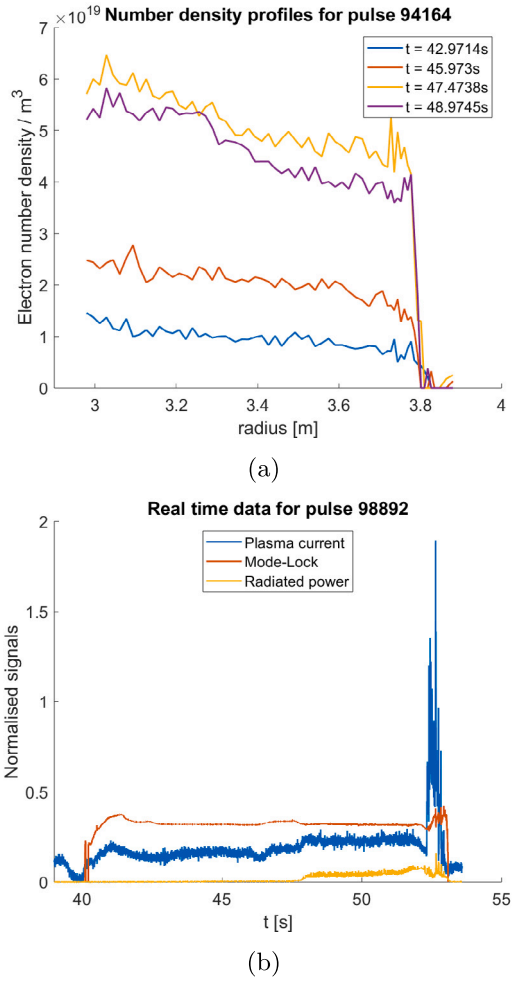

Fig. 7. Plots show an example of electron number density profiles 7(a) over the torus at four different times and the evolution over time of three normalised real time signals 7(b) over time.

4.1. Fluctuations of intensities in the mask method

Since the mask method hinges upon the average intensity values within each mask, a straightforward assessment of the mean intensity passed from the divertor to the MARFE detection mask can be performed. For this purpose, the average intensity of the divertor mask is subtracted from the divertor mask in the frame in which the MARFE has been detected. The absolute values of these intensity differences have been meticulously illustrated in Fig. 8 alongside their disruptional behaviour.

MARFE detections with intensity shift values exceeding 100 (mean pixel intensity) are observed to be disruptive, characterised by exceptionally bright and rapid MARFE events or instances where video recordings experienced issues like a complete white screen. Conversely, non-disruptive MARFEs typically exhibit low intensity shifts, indicating a relatively dim region within the mask that still qualifies as a MARFE. These cases, often referred to as 'soft MARFEs' or 'soft-landing MARFEs' in JET log files, are characterised by slow MARFE progression, frequently occurring near the divertor.

4.2. Intensity loss at divertor area

Examining the data from the ROI closest to the divertor (light blue in Figs. 4 and 6(b)) in comparison with the mean intensity after the MARFE for can give information regarding how sudden the shift in

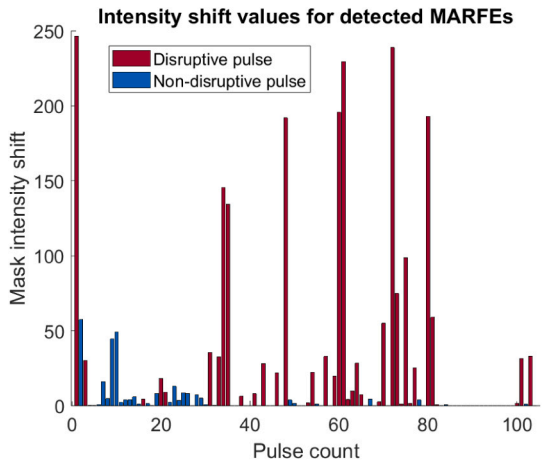

Fig. 8. Figure shows a bar plot with the intensity shifts detected. The red bars indicate that the given pulse was disruptive.

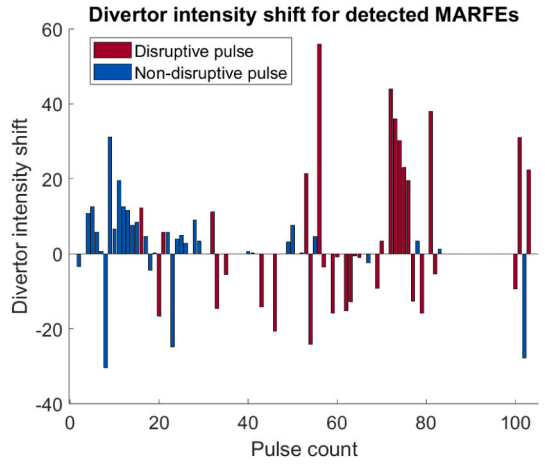

Fig. 9. The bar plot depicts the intensity shift values for the divertor area for the MARFE pulses in the database.

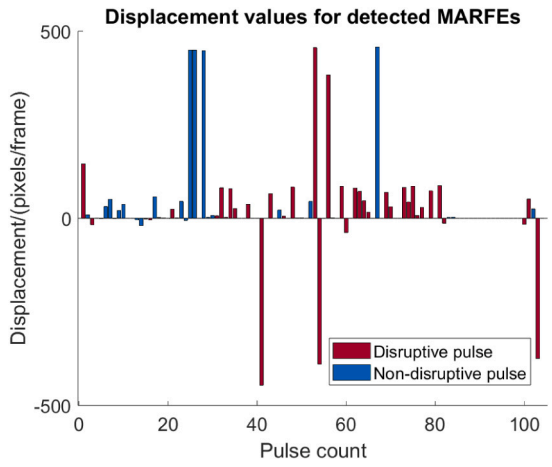

Fig. 10. Bar plot shows the different values for the displacement vector (in pixels/frames) for pulses with MARFE for both disruptive and non-disruptive pulses.

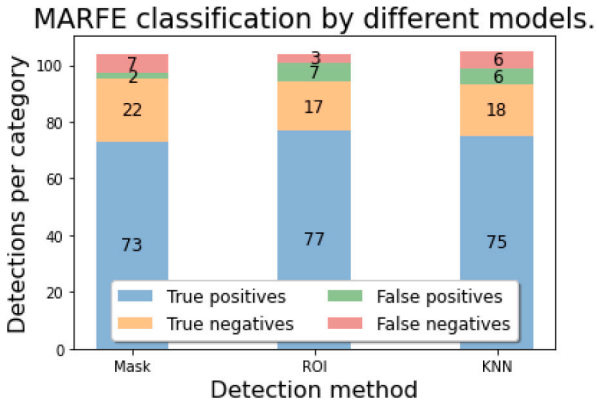

Fig. 11. The graph shows the results obtained for each method in classifying MARFE based on videos.

intensity was in the moment of the detection. Fig. 9 shows the results for the database, emphasising between disruptive and non-disruptive pulses.

Again, it can be seen that all the pulses with an intensity shift greater than a certain value are always disruptive. In addition, it should be noted that all pulses with MARFE and with a negative value (cases in which the divertor value did not decrease right after the detection) are non-disruptive. Sadly, there are not enough occurrences of this phenomenon to properly study it in this database.

4.3. KNN regions analysis

As stated in 2.3, the KNN approach is based in both the mean intensity of the HF and the results obtained from running a KNN region algorithm in each frame. Given that the previous methods have already employed intensity shifts in a more comprehensive manner, the focus of comparison will now be on the modulus of the displacement vector. Fig. 10 shows the displacement vector (in pixels/frame) of the main centroid of the first frame with MARFE according to the KNN method.

The most noticeable result is the clear correlation between the obtained negative values with disruptive pulses. A negative value, in this context, indicates that after a fast movement of the region centroid over the frame, it remained in the same position, which would indicate a very fast radiation flux that stays localised in the nearby area of the video frames. Similarly to the case with the divertor's intensity shift, there are not enough pulses in which this happens to make a statistically relevant conclusion.

4.4. Results for classification

In Fig. 11 the classification outcomes for individual pulses derived from the three primary approaches are presented. The figure illustrates the distribution of True Positives (TP; the MARFE was properly detected), False Positives (FP; there was a detection, but no MARFE was identified), True Negatives (TN; no detection and there was not a MARFE), and False Negatives (FN; no detection, but it was labelled as a MARFE occurrence) within the dataset returned by each model not based on Machine Learning. In order to consider a proper detection, the returned times must partially overlap with the detection times found when creating the database.

The overall accuracy values of each method are 0.885 for the KNN method, 0.904 for the ROI method and finally, 0.914 for the mask-based approach. These accuracy scores have been calculated using Eq. (1), where N is the number of predictions.

$$acc = \frac{TP + TN}{N} \tag{1}$$

The three techniques score similarly but interestingly enough have some visible differences when comparing their confusions matrix values.

Regarding the Machine Learning models, the accuracy for training and testing for each model can be found in Table 1.

Table 1
Table shows the results for the Machine Learning models. The second Video-based model (marked with *) stands for the video-based model without any data from the KNN model in its feature vectors.

Model	Train acc. (%)	Test acc. (%)
Binary model	93.2	90.3
Video based	94.7	94.6
Video based*	93.2	94.2
Comprehensive	98.4	96.9

Table 2
Table shows the results for the True Positives, True Negatives, False Positives and False Negatives for the different Machine Learning techniques for the testing dataset. Again, Video based* stands for the video based model without data from the KNN model.

Model	TP	TN	FP	FN
Binary model	21	7	3	0
Video based	244	282	3	7
Video based*	239	272	5	15
Comprehensive	206	227	2	4

Table 3
Table shows the results for the prediction of MARFEs and soft-landed MARFEs. Again, the second video-based* model stands for the model without KNN-region analysis data in its feature vectors.

Model	Arch.	Train acc. (%)	Test acc. (%)
Video based	SVM	95.5	91.2
Video based*	SVM	94.6	93.3
Comprehensive	KNN	99.3	98.0

Table 2 shows in a more detailed way the distribution of TP, TN, FP and FN of the Machine Learning techniques for the testing data.

After conducting thorough tests on the aforementioned classification methods and achieving satisfactory results, a subsequent experiment was formulated to assess the capability of these models in distinguishing between the two types of MARFEs: the soft landed MARFEs (described briefly in 4.1) and the ones more likely to disrupt the plasma, which are also more common.

Following the scheme in Table 1, three different models were created: two based solely on video data (including and excluding the inputs from the model based on KNN-generated regions) and a final model with all 166 feature vectors (as in 3.3). The results for the architecture and accuracy in the training and testing sets can be found in Table 3. The base dataset for the training of these models is the same as the one used for the training of each model for the Machine Learning methods previously described. The only major change is that the target variable now differentiates between no MARFE, MARFE and the soft-landed MARFE. Again, the architecture and hyper-parameters were obtained via optimisation functions.

Fig. 12 shows the confusion matrices for all the three classification models for no MARFE (marked as 0), MARFEs (labelled as 1) and soft-landed MARFEs (labelled as 2). While the prediction results are outstanding, more inputs for soft-landed MARFEs can be added to improve the database.

5. Conclusions

This work summarises key findings achieved by establishing a MARFE database from JET pulses and analysing operational camera data, resulting in effective MARFE classification. These outcomes emphasise the significance of operational cameras for detection and suggest broader applicability, including for tokamaks like ITER or JT-60SA.

In this research, three methods were used to classify MARFEs: applying masks to frames with a 91.4% accuracy, analysing Regions of Interest with 90.4% accuracy (as previously published), and tracking KNN-formed regions with 88.46% accuracy, albeit computationally intensive.

These methods not only offer accuracy but also valuable insights into the discharge process. For example, the mask-based approach examined average intensity differences between the High Field and divertor regions during MARFEs, revealing a disruptive behaviour threshold. Additionally, tracing the intensity centroid's movement aids in identifying the main intensity blob and studying radiation flux dynamics.

The data produced by the previous methods and their outputs was used to create Machine Learning models. The first model utilised a kernel logistic regression architecture and binary results from the MARFE detectors as inputs, achieving a test accuracy of 90.1% for classifying discharges. However, this model did not demonstrate significant improvement over non-statistical approaches regarding pulse classification.

The second model utilised all the frame-by-frame information from intermediate files generated by the non-statistical techniques to create a comprehensive video dataset. This dataset was used to train a neural network model, enabling frame-by-frame prediction of MARFEs with a test accuracy of 94.6%. To address the computational demands of the KNN-based approach, a secondary neural network was designed using inputs solely from the mask and ROI methods, resulting in a test accuracy of 94.2%.

These results indicate that the video data obtained from JET's operational cameras is a reliable and valuable source of information for MARFE detection.

The third and final Machine Learning model, utilising a KNN-based architecture, incorporated data from previous videos alongside other JET instruments and diagnostics to create a new dataset of 166 feature vectors. This model achieved the highest testing accuracy for MARFE detection with a score of 96.9% in time steps of ms.

Additionally, extra Machine Learning models were created to differentiate between MARFEs and soft-landed MARFEs, not linked with disruptional behaviour, obtaining excellent results. For video only models similar in database design to the ones previously described, a test accuracy of 93.3% was obtained. Another 'comprehensive' model with 166 distinct feature vectors was created emulating the first dataset that incorporated additional JET signals, which obtained a final test score of 98%.

6. Future work

After reviewing the technique explained in this work, it is evident that they offer distinct advantages for effective implementation with existing technology. To enhance and apply these techniques further, three discernible avenues are proposed:

1. Real-Time Validation: A crucial step forward involves subjecting the carefully developed models to rigorous real-time scenarios that encompass a diverse range of JET discharges. This robust validation process will aim to definitively establish their suitability for direct integration into real-time operations, mirroring the well-established PETRA framework.
2. Expanding the MARFE Database: Notably, the methodologies, particularly those rooted in Machine Learning, have demonstrated remarkable effectiveness when exclusively applied to video files. Thus, a practical avenue for progress involves decisively expanding the MARFE database by incorporating video files exclusively. This focused approach promises to significantly enhance the database's reach and utility.
3. Database Enrichment and Rigorous Statistical Validation: A pivotal stride involves resolutely expanding the existing database, coupled with a thorough and comprehensive statistical validation of the conclusions drawn in the preceding section. This determined effort serves as a strong means to substantiate and underscore the robustness and profound significance of the derived insights.

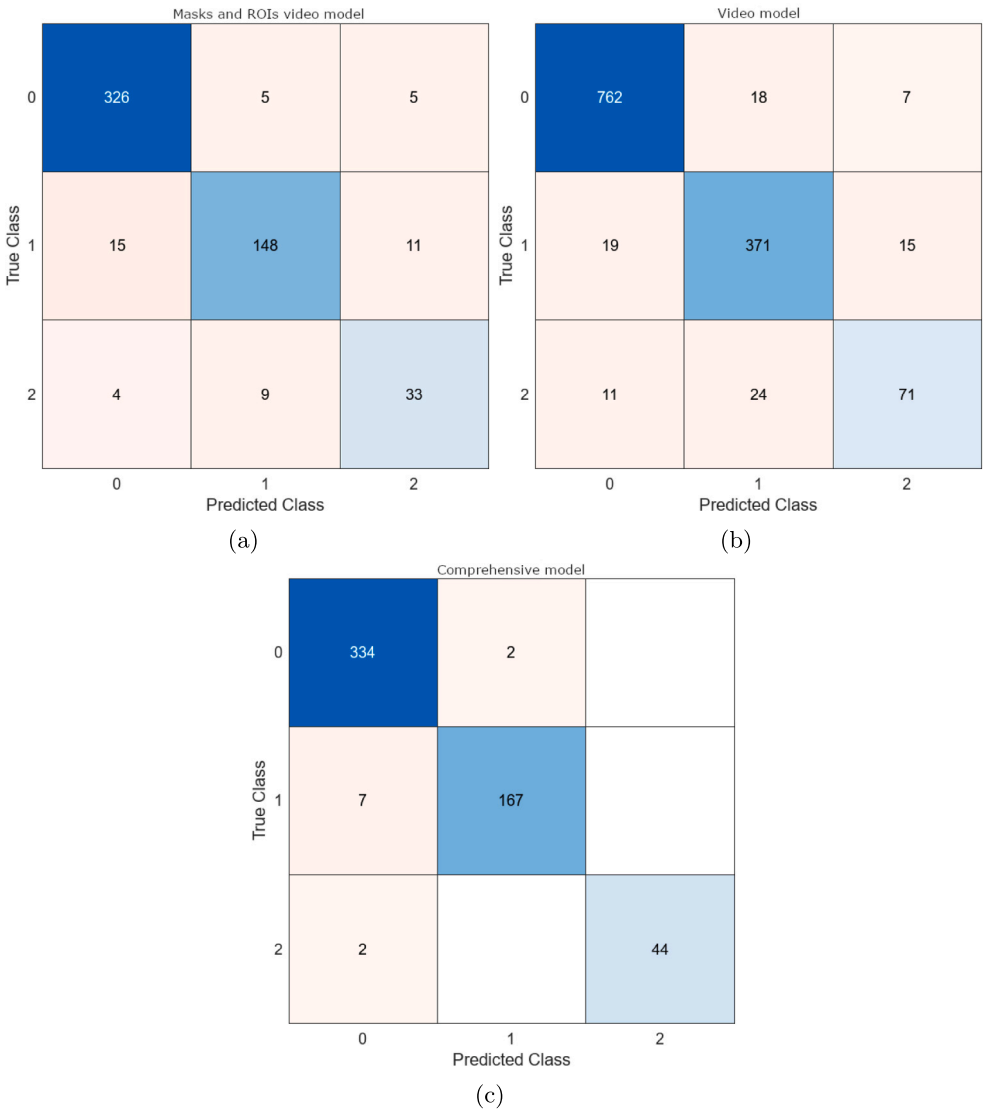

Fig. 12. Confusion matrices obtained for the mask and ROI model (a), full video model (b) and the model with all 166 feature vectors (c).

4. Possible correlations with other phenomena: given that it is possible to expand the database and obtain good timings for the occurrence of the MARFE, it is now possible to find whether or not there are possible correlations between MARFEs and other unused signals/physical phenomena, such as external heating or more concise discharge configurations.
5. Investigate potential associations between MARFE events and the device's mechanical configuration, encompassing valve type and specific fuelling gas conditions. This aligns with the previous suggestion of exploring correlations between MARFE and other signals.

CRediT authorship contribution statement

A. González Ganzábal: Data curation, Formal analysis, Investigation, Methodology, Software, Visualization, Writing – original draft, Writing – review & editing. **G.A. Rattá:** Conceptualization, Investigation, Resources, Software, Validation, Writing – review & editing. **D. Gadariya:** Data curation, Software, Writing – review & editing. **S. Dormido-Canto:** Conceptualization, Supervision, Writing – review & editing.

Declaration of competing interest

The authors declare that they have no known competing financial interests or personal relationships that could have appeared to influence the work reported in this paper.

Data availability

Data will be made available on request.

Acknowledgements

This work was supported in part by the Spanish Ministry of Science, Innovation and Universities under Projects PID2022-137680OB-C31, PID2019-108377RB-C31 and PID2022-137680OB-C32.

This work has been carried out within the frame- work of the EUROfusion Consortium, funded by the European Union via the Euratom

Research and Training Programme (Grant Agreement No 101052200 - EUROfusion). Views and opinions ex- pressed are however those of the author(s) only and do not necessarily reflect those of the European Union or the European Commission. Neither the European Union nor the European Commission can be held responsible for them.

Appendix A. List of signals

The different real time signals from other JET instruments were saved in individual files per discharge. The following list details each variable and the node from the JDC that contains each set. Each node indicates the path used to download the signal using the *jetdsp* application found in JET's machines. More information regarding the data and metadata of each signal can be obtained through the JET Dashboard or the Simple Access Layer (SAL), the JET API for Python. Additional details are present in JET's Data Handbook.

1. Plasma Current (XG/RTSP/KC1IPLA)
2. ModeLock (XG/RTSP/LOCA)
3. Plasma Internal Inductance (xg/rtss/LI)
4. Plasma Density (XG/RTSS/Ne1KG1)
5. Poloidal Beta (XG/RTSS/BPDIA)
6. Total Input Power (XG/RTSS/PTOT)
7. Plasma Vertical Position (XG/RTSS/ZCC)
8. Radiated Power (XG/RTSS/KB5Ptot)
9. Stored diamagnetic energy derivative (XG/RTSS/FDWDT)
10. Bolometry signal for Core plasma lower section. The bolometry data comes from KB5 diagnostic and corresponds to the calibrated radiation power (jpf/db/B5HR-PBOL:014)
11. Bolometry signal for Core plasma upper section (jpf/db/B5HR-PBOL:015)
12. Bolometry signal for lower section (jpf/db/B5HR-PBOL:010)
13. Bolometry signal for upper section (jpf/db/B5HR-PBOL:020)
14. Vertical Soft X-ray Core plasma measurement signal. Signal in amperes, from KJ34. This applies to all following Vertical Soft X-ray signals (jpf/db/J4-SXR<T09)
15. Vertical Soft X-ray High Field Side measurement signal (jpf/db/J4-SXR<T02)
16. Vertical Soft X-ray High Field Side measurement signal (JPF/DB/J4-SXR<T03)
17. Vertical Soft X-ray Low Field Side measurement signal (JPF/DB/J4-SXR<T26)
18. Vertical Soft X-ray Low Field Side measurement signal (JPF/DB/J4-SXR<T27)
19. High Field Side Line Integrated Density Signal. Taken from KG4. Units in m^{-2}. Applies to all integrated densities (JPF/DF/G1R-LID:001)
20. Core Plasma Line Integrated Density Signal (JPF/DF/G1R-LID:002)
21. Core Plasma Line Integrated Density Signal (JPF/DF/G1R-LID:003)
22. Low Field Side Line Integrated Density Signal (JPF/DF/G1R-LID:004)
23. Real time signal of Total ICRH Power used for the discharge (XG/RFLM/PL)
24. Processed signal of Total ICRH Power used for the discharge (not to be mistaken with the one above); (PPF/ICRH/PTOT)
25. Plasma Diamagnetic Energy (JPF/GS/BL-WDIA<S)
26. Plasma MHD Energy (JPF/GS/BL-WMHD<S)
27. Plasma Total Energy (can be found either at JPF/XG/RTSS/WTOT or at JPF/XG/RTSP/WTOT)
28. Jump to Termination signal. Not to be confused with the JTT stop from JET's Dashboard (JPF/XG/RTSP/RtpsJTT)

Appendix B. List of acronyms

The list of acronyms used in this work are the following:

- *CCD:* Charge-Couple Device
- *FN:* False Negative
- *FP:* False Positive
- *HF:* High Field
- *ICRH:* Ion Cyclotron Resonance Heating
- *ILA:* ICRF Load-tolerant antenna
- *IWGL:* Inner Wall Guard Limiter
- *JDC:* JET Data Centre
- *JET:* Joint European Torus
- *KNN:* K-Nearest Neighbour
- *LBFGS:* Limited-memory Broyden–Fletcher–Goldfarb–Shanno algorithm
- *MARFE:* Multifacetic Asymmetric Radiation From the Edge
- *PETRA:* Plasma Events TRiggering Alarm
- *RFA/RFB* Radio Frequency systems for ion cyclotron range of frequencies, a heating system
- *ROI:* Region Of Interest
- *RTPS:* Real Time Protection Sequencer
- *SAL:* Simple Access Layer
- *TN:* True Negative
- *TP:* True Positive
- *UDPT:* Upper Dump Plate Tiles
- *UIWP:* Upper, Inner Wall Protections

References

[1] B. Lipschultz, B. LaBombard, E.S. Marmar, M.M. Pickrell, J.L. Terry, R. Watterson, S.M. Wolfe, MARFE: An edge plasma phenomenon, Nucl. Fusion 24 (8) (1984) 977–988.

[2] Peng Shi, G. Zhuang, K. Gentle, Qiming Hu, Jie Chen, Qiang Li, Yang Liu, Li Gao, Xiaolong Zhang, Hai Liu, Zhipeng Chen, Lizhi Zhu, Fuming Li, Yinan Zhou, Zhong Zeng, Linzi Liu, Jiyang He, First time observation of local current shrinkage during the MARFE behavior on the J-TEXT tokamak, Nucl. Fusion 57 (11) (2017) 116052.

[3] G.A. Rattá, J. Vega, A. Murari, D. Gadariya, JET Contributors, PHAD: a phase-oriented disruption prediction strategy for avoidance, prevention, and mitigation in JET, Nucl. Fusion 61 (11) (2021).

[4] T. Craciunescu, A. Murari, I. Tiseanu, J. Vega, JET-EFDA Contributors, Phase congruency image classification for MARFE detection on JET with a carbon wall, Fusion Sci. Technol. 62 (2) (2012) 339–346.

[5] L. Spolladore, R. Rossi, I. Wyss, P. Gaudio, A. Murari, M. Gelfusa, Detection of MARFEs using visible cameras for disruption prevention, Fusion Eng. Des. 190 (2023) 113507.

[6] Valentina Huber, Alexander Huber, David Kinna, Guy Matthews, Itziar Balboa, Adrian Capel, Paul McCullen, Philippe Mertens, Gennady Sergienko, Scott Silburn, Klaus-Dieter Zastrow, JUVIL: A new innovative software framework for data analysis of JET imaging systems intended for the study of plasma physics and machine operational safety, Fusion Eng. Des. 123 (2017) 979–985.

[7] JET Data Wiki, CJET viewing systems, 2024, https://wiki.jetdata.eu/open/index.php/JET_viewing_systems#Views. (Online; accessed 30-January-2024).

[8] JET Data Wiki, Camera views for KL7-P8WA and KL1-O8WA, 2023, https://wiki.jetdata.eu/open/images/5/56/KL7_model.png. (Online; accessed 17-July-2023).

[9] G.A. Rattá, J. Vega, A. Murari, D. Gadariya, C. Stuart, G. Farías, Characterization of physics events in JET preceding disruptions, Fusion Eng. Des. 189 (2023) 113468.

[10] C.I. Stuart, G. Artaserse, P. Card, I.S. Carvalho, R. Felton, S.N. Gerasimov, A. Goodyear, R.B. Henriques, D. Karkinsky, P.J. Lomas, P. McCullen, F. Rimini, A.V. Stephen, D.F. Valcárcel, J. Waterhouse, M. Wheatley, PETRA: A generalised real-time event detection platform at JET for disruption prediction, avoidance and mitigation, Fusion Eng. Des. 168 (2021) 112412.

[11] J. Gareth, D. Witten, T. Hastie, R. Tibshirani, An introduction to statistical learning with applications in R: by Gareth James, Daniela Witten, Trevor Hastie, and Robert Tibshirani, New York, Springer Science and Business Media, 2013, $41.98, eISBN: 978-1-4614-7137-7, Stat. Theory Relat. Fields 6 (1) (2022) 87.

[12] MAthWorks, Noise removal, 2020, https://es.mathworks.com/help/images/noise-removal.html. (Online; accessed 10-April-2023).